



Cite this: *Nanoscale*, 2025, **17**, 5981

## Ferroelectricity enhances ion migration in hard carbon anodes for high-performance potassium ion batteries†

Li Rui,<sup>a</sup> An Keyu,<sup>a</sup> Ouyang Hao,<sup>a</sup> Li Heng,<sup>id</sup> \*<sup>b</sup> Zhang Yanyan,<sup>id</sup> <sup>c</sup> Tang Yuxin,<sup>id</sup> <sup>c</sup> Liu Jilei<sup>id</sup> <sup>d</sup> and Chen Shi<sup>id</sup> \*<sup>a</sup>

Hard carbon is a promising candidate for potassium ion batteries due to its large interlayer spacing and abundant closed pores. However, the slow migration and sluggish diffusion kinetics of potassium ions lead to inferior insertion and pore-filling processes, causing severe ion channel blocking, continuous byproduct generation, and poor cycling stability. In this study, we coated hard carbon on top of tetragonal barium titanate particles forming a ferroelectricity-aided anode (t-BTO@C). The t-BTO@C anode exhibits higher interfacial charge density, enhanced insertion-pore filling capacity, and formation of fewer byproducts. The effective interaction between the spontaneous polarization electric field of t-BTO and potassium ions accelerates the potassium ion kinetics and ensures the homogeneous migration of potassium ions, as well as the improvement of t-BTO@C anode potassium storage. After 100 cycles at 0.05 A g<sup>-1</sup>, the t-BTO@C anode shows a specific capacity of 374.9 mA h g<sup>-1</sup>, higher than those of SiO<sub>2</sub>@Carbon (97.2 mA h g<sup>-1</sup>) and Pure Carbon (240.1 mA h g<sup>-1</sup>). Paired with a Prussian white cathode, the full cell shows a specific capacity of 313.0 mA h g<sup>-1</sup> at 0.1 A g<sup>-1</sup>, with 88.9% capacity retention after 40 cycles, much higher than those in recent reports. Our strategy provides a new path to improve the performance of the hard carbon anode in potassium ion batteries.

Received 22nd November 2024,

Accepted 8th January 2025

DOI: 10.1039/d4nr04916k

rsc.li/nanoscale

## 1. Introduction

Hard carbon is a potential candidate for alkali ion storage due to its larger interlayer spacing compared to graphite and abundant active sites for ion anchoring.<sup>1</sup> It is particularly suitable for batteries with larger ions, like sodium ion batteries (SIBs) and potassium ion batteries (PIBs). SIBs with hard carbon anodes have already been commercialized. Nevertheless, hard carbon in PIBs still faces many fundamental problems.<sup>2</sup> Due to the large size of potassium ions (1.38 Å for K<sup>+</sup>), the hard carbon anode suffers from large structural deformation and ion channel blocking, causing fast capacity decay.<sup>3,4</sup> Due to

their large atomic mass, potassium ions show sluggish ion diffusion kinetics and cause poor rate performance in PIBs.<sup>5</sup> Meanwhile, the sluggish kinetics also cause large polarization at the interface, causing continuous solid electrolyte interphase (SEI) formation and byproduct generation.<sup>3</sup> The storage of potassium ions in hard carbon can be described using a two-stage model. The first stage is the adsorption of potassium ions on the surface active sites indicated by a steep slope region in the voltage-capacity graph above 1 V vs. K<sup>+</sup>/K. The second stage is insertion-pore filling into the interlayers and nanopores of hard carbon, shown as a relatively flat region with a voltage below 1 V vs. K<sup>+</sup>/K.<sup>6</sup> The sluggish diffusion kinetics mostly affect the insertion-pore filling stage, which can be seen from the shortened capacity near 0 V vs. K<sup>+</sup>/K.<sup>7</sup> There are several approaches for addressing the obstacles in ion migration including enlarging the graphitic interlayer spacing and enhancing electronic conductivity by doping heteroatoms<sup>8,9</sup> (sulfur, phosphorus, nitrogen, etc.) or engineering mesoporous structures to shorten the potassium ion migration distance.<sup>10</sup> For example, Chen *et al.* designed a sulfur/oxygen co-doped porous hard carbon microsphere anode with an enlarged interlayer distance and abundant structural defects, which delivers 226.6 mA h g<sup>-1</sup> at 0.05 A g<sup>-1</sup> over 100 cycles.<sup>8</sup> Cheng *et al.* constructed 3D honeycomb-like porous carbon with rapid de/intercalation kinetics of potass-

<sup>a</sup>Joint Key Laboratory of the Ministry of Education, Institute of Applied Physics and Materials Engineering, University of Macau, Macau 999078, China.

E-mail: shichen@um.edu.mo

<sup>b</sup>State Key Laboratory of High-Performance Ceramics and Superfine Microstructure, Shanghai Institute of Ceramics, Chinese Academy of Sciences, Shanghai 200050, P. R. China. E-mail: liheng@mail.sic.ac.cn

<sup>c</sup>College of Chemical Engineering, Fuzhou University, Fuzhou 350116, P. R. China

<sup>d</sup>College of Materials Science and Engineering, Hunan Joint International Laboratory of Advanced Materials and Technology of Clean Energy, Hunan Province Key Laboratory for Advanced Carbon Materials and Applied Technology, Hunan University, Changsha, 410082 Hunan, P.R. China

† Electronic supplementary information (ESI) available. See DOI: <https://doi.org/10.1039/d4nr04916k>



ium ions, delivering 456 mA h g<sup>-1</sup> at 0.05 A g<sup>-1</sup> over 10 cycles.<sup>10</sup> However, these methods could only enhance potassium ion migration passively.

Ferroelectricity is a phenomenon that materials have spontaneous electric polarization in a non-centrosymmetric lattice structure. In these materials, there are two metastable states with opposite internal dipole directions, which can be switched using an external electric field (Fig. S1†). One such example is the tetragonal barium titanate (t-BTO). In t-BTO lattices, Ti<sup>4+</sup> is bonded with six O<sup>2-</sup> forming corner shared octahedral TiO<sub>6</sub><sup>2-</sup> cages. When the lattice is deviated from the cubic phase, the cage is elongated in the z direction and allows Ti<sup>4+</sup> to have two equivalent positions in the cage. As a result, in a tetragonal BTO crystal, the two sub-lattices have opposite dipole moments. This intrinsic dipole moment in the t-BTO crystal lattice (spontaneous polarization,  $P_s$ ) could spontaneously form randomized polarization domains, which can enhance the localized electric field to accelerate ion migration. By applying an external coercive field, the t-BTO lattice could be polarized and show a strong persistent electric field.<sup>11–14</sup> The ferroelectric materials were reported in lithium ion batteries as an effective strategy to regulate ion deposition.<sup>15</sup> Sun *et al.* used ferroelectric t-BTO in polyethylene oxide-based composite polymer electrolytes to increase lithium ion transport.<sup>16</sup> Xia *et al.* used the t-BTO layer to regulate lithium ion deposition and suppress dendrites. With horizontally polarized t-BTO, the deposition direction of lithium preferentially changed from vertical to lateral.<sup>17</sup> In PIBs, there are only a few papers using ferroelectric particles in separators or solid electrolytes to enhance ion migration.<sup>18,19</sup> Wang *et al.* used ferroelectric particles in the separator to regulate potassium ion deposition in anode-free PIBs.<sup>19</sup> However, there is no report on the regulation of potassium ion kinetics inside the hard carbon anode, which could be more direct and effective.

Herein, we successfully accelerated potassium ion kinetics in the hard carbon anode by coating it on top of ferroelectric t-BTO particles. The t-BTO particles show a maximum spontaneous polarization  $P_s$  of 3.46  $\mu\text{C cm}^{-2}$ . The ferroelectric field of t-BTO particles successfully enhanced potassium ion kinetics and showed higher capacity in the insertion-pore filling stage. After 100 cycles at 0.05 A g<sup>-1</sup>, the t-BTO@C anode shows a specific capacity of 374.9 mA h g<sup>-1</sup>, higher than those of SiO<sub>2</sub>@Carbon (97.2 mA h g<sup>-1</sup>) and Pure Carbon (240.1 mA h g<sup>-1</sup>). At 1 A g<sup>-1</sup> for 1000 cycles, the t-BTO@C anode retained 82.8% of its capacity at the 20th cycle, while the SiO<sub>2</sub>@Carbon (SiO<sub>2</sub>@C) completely lost all its capacity. In addition, t-BTO@C also showed much less byproduct generation. SEM and AFM images revealed that the t-BTO@C anode shows the most uniform and stable SEI layer without byproducts in 100 cycles. By pairing with the Prussian White (PW) cathode, the full-cell exhibits an initial discharge specific capacity of 356.2 mA g<sup>-1</sup> at a current density of 0.05 A g<sup>-1</sup>. After 40 cycles, the full cell retains 313.0 mA g<sup>-1</sup> discharge specific capacity with 88.9% capacity retention compared to the 10th cycle. Our findings provide a new strategy to enhance the capacity and stability of PIBs.

## 2. Experimental section

### 2.1. Synthesis of t-BTO particles

t-BTO was synthesized by hydrothermal methods. Tetrabutyl titanate, barium hydroxide, aqueous ammonia, and deionized water were placed in the autoclave with a barium and titanium ratio of 2 : 1, holding at 200 °C for 36 hours. After the reaction, the products were centrifugally washed with acetic acid, deionized water, and anhydrous ethanol, followed by annealing at 80 °C in a vacuum-drying oven for 12 hours. The powder was ground to obtain t-BTO particles.<sup>20,21</sup>

### 2.2. Synthesis of t-BTO@C, SiO<sub>2</sub>@C, and Pure Carbon particles

70 mg of t-BTO was added in a certain amount of deionized water, and hexadecyl trimethyl ammonium bromide. The mixture was sonicated for 1 hour. An additional 8 ml of ethylene glycol and 0.9 ml of pyrrole were added to the solution followed by reaction at 0–4 °C for 24 hours. The product was filtered, washed, and dried at 80 °C for 12 hours to obtain t-BTO@polypyrrole particles. t-BTO@polypyrrole particles were placed in a ceramic boat and held under an argon atmosphere at 800 °C for 2 hours for carbonization, to obtain t-BTO@C. SiO<sub>2</sub>@C powder was obtained using the same sequence, and Pure Carbon (Pure C) was synthesized without the addition of t-BTO.<sup>22–24</sup>

### 2.3. Synthesis of PW particles

PW was synthesized using the co-precipitation method. Typically, 1.12 g of iron sulfate heptahydrate, 5 g of potassium citrate, 15 g of potassium chloride, and 0.88 g of ascorbic acid were dissolved in 100 ml of deionized water as solution A under a nitrogen atmosphere. Additionally, 1.69 g of potassium ferrocyanide trihydrate was dissolved in 100 ml of deionized water as solution B. Solution B was added dropwise to solution A at a rate of 0.28 ml min<sup>-1</sup> using a peristaltic pump under a nitrogen atmosphere. The milky-white product was left to stand overnight, washed three times by centrifugation using deionized water, and finally freeze-dried for 48 hours to obtain the Prussian white powder.<sup>25,26</sup>

### 2.4. Synthesis of the t-BTO film

0.06 g of barium acetate and 0.08 g of isopropanol titanate were dissolved in 2 mL of a solvent which was a mixture of acetic acid, ethanol and deionized water, and this is referred to as solution 1. 40  $\mu\text{L}$  of solution 1 was sucked up and spin-coated on 16 mm copper foil, with an acceleration of 2000 rpm, for 30 s. The spin coater copper foil was held in a vacuum tube furnace at 1000 °C for 2 h, to obtain the t-BTO film.

## 3. Results and discussion

t-BTO nanoparticles were synthesized by the hydrothermal method.<sup>21</sup> As shown in Fig. 1a and b, the t-BTO nanoparticles



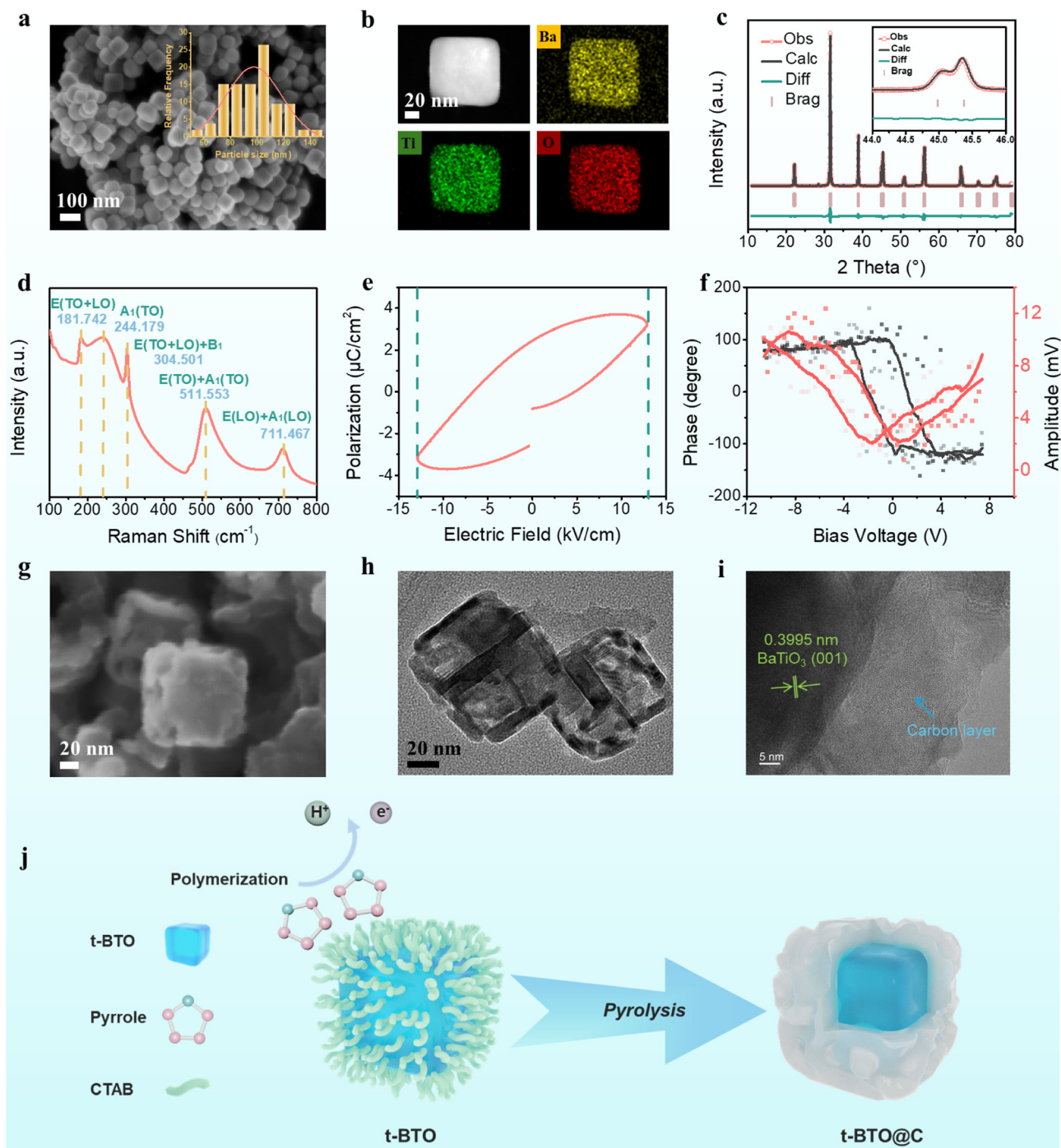


**Fig. 1** (a) SEM image and particle size distribution (insert image) of t-BTO nanoparticles. (b) HAADF-STEM image and distribution of Ba, Ti, and O elements of t-BTO nanoparticles. (c) The XRD curve of t-BTO nanoparticles and a localized zoomed-in view. (d) Raman spectroscopy of t-BTO nanoparticles. (e) The  $P$ - $E$  hysteresis loop of t-BTO nanoparticles. (f) The phase (black line)/amplitude (red line)-voltage loop of t-BTO nanoparticles. (g) SEM image of t-BTO@C materials. (h) and (i) high-resolution TEM image of t-BTO@C materials. (j) Synthetic scheme of t-BTO@C materials.

have a cube-like shape with a size of about 50–150 nm, with a median at 100 nm. Powder X-ray diffractogram (XRD) profiles show that the calculated profiles were indexed to the space group of  $P4mm$  t-BTO (PDF#75-0462) with  $a = b = 3.995 \text{ \AA}$  and  $c = 4.028 \text{ \AA}$  (Fig. 1c). There is a split of diffraction peak in  $2\theta = 45.25^\circ$  shown in the inset of Fig. 1c, matching the (200) and

(002) crystal planes in PDF#75-0462. Due to the elongation along the  $z$  direction, the diffraction peaks of the (200) and (002) crystal planes were no longer equal. This is a characteristic feature of the tetragonal phase of the BTO lattice.<sup>20</sup> Further evidence of the tetragonal ferroelectric phase can be found in the Raman spectra. Three vibration modes ( $A_1$ , E,



and  $B_1$ ) in the tetragonal phase are Raman active and observed in Fig. 1d. The sharp peak near  $181.7\text{ cm}^{-1}$  corresponds to the  $E(\text{TO})$  and  $E(\text{LO})$  modes, and the broad peak at  $244.2\text{ cm}^{-1}$  is from the  $A_1(\text{TO})$  mode. The sharp peak at  $304.5\text{ cm}^{-1}$  is due to the  $E(\text{TO})$ ,  $E(\text{LO})$  and  $B_1$  modes. The peaks at  $511.6$  and  $711.5\text{ cm}^{-1}$  correspond to the  $E(\text{TO})$ ,  $A_1(\text{TO})$ , and  $E(\text{LO})$ ,  $A_1(\text{LO})$  modes, respectively.<sup>27</sup> These results indicate that the  $\text{Ti}^{4+}$  and  $\text{O}^{2-}$  of t-BTO deviate from the center of the primitive cell, confirming that the t-BTO particles are in the tetragonal phase. The magnitude of ferroelectricity was measured by ferroelectric hysteresis as shown in Fig. 1e. The  $P$ - $E$  hysteresis loop shows that  $P_s$  was  $3.46\text{ }\mu\text{C cm}^{-2}$ , the remanent polarization ( $P_r$ ) was  $2.47\text{ }\mu\text{C cm}^{-2}$ , and  $E_c$  was  $13.16\text{ kV cm}^{-1}$ . From the size distribution of t-BTO polycrystalline particles, the maximum switch voltage was  $6.58 \times 10^{-2}$ – $1.97 \times 10^{-1}\text{ V}$ , which might be spontaneously switched during potassiation/depotassiation. Piezoresponse force microscopy (PFM) was used to verify the ferroelectricity of the particles at the microscopic scale. In Fig. 1f, the  $180^\circ$  phase shifts and butterfly amplitude loops strongly confirm the ferroelectricity of t-BTO polycrystalline particles. It can be seen that the maximum forward switch voltage in the phase profiles is  $3.51\text{ V}$ , and the maximum reverse switch voltage is  $3.39\text{ V}$ . The average maximum switch voltage is  $3.45\text{ V}$ . Similarly, the  $180^\circ$  phase contour map detects the polarization reversal of the ferroelectric domains when the bias changes from  $3\text{ V}$  to  $-3\text{ V}$  (Fig. S3a–c).<sup>†</sup> Most of the ferroelectric domains in the t-BTO nanoparticle distribution region are in the  $180^\circ$  phase when the bias voltage is  $3\text{ V}$ , and most of the ferroelectric domains in the t-BTO nanoparticle are switched to the  $0^\circ$  phase when the bias voltage is  $-3\text{ V}$ .<sup>28,29</sup> The PFM measurement confirmed the ferroelectricity in t-BTO particles.

The XRD curve of t-BTO@C shown in Fig. S4a<sup>†</sup> displays a wide peak at around  $2\theta = 20^\circ$ , representing the characteristic peak of the graphitic carbon (002) crystal plane. The broadening of this peak suggests a disordered carbon lattice, which is commonly observed in hard carbon.<sup>30,31</sup> The diffraction peak located at  $2\theta = 45.25^\circ$  for t-BTO as depicted in Fig. S4b<sup>†</sup> still manifests a bifurcation into a pair of diffraction peaks. The core-shell structure of t-BTO@C was confirmed through the use of a Scanning Electron Microscope (SEM) and a Transmission Electron Microscope (TEM). As shown in the SEM image (Fig. 1g), the surface of the smooth cubic t-BTO particles roughens due to the hard carbon coating. The TEM images (Fig. 1h and i) clearly reveal the hard carbon shells outside the t-BTO cores. In comparison,  $\text{SiO}_2$ @C shows a similar core-shell structure while the Pure C sample shows the amorphousness of hard carbon (Fig. S5<sup>†</sup>). The lattice pattern of the core layer corresponds to the (001) crystal plane of t-BTO, whereas the carbon layer is observed as a continuous layer with a thickness ranging from  $10$  to  $20\text{ nm}$ . In addition, the TEM energy dispersive spectra (EDS) shown in Fig. S6<sup>†</sup> reveal that Ba and Ti elements are uniformly distributed in the core layer, while C elements are dispersed throughout the entire particle. This evidence implies that the t-BTO nanoparticles remain in the tetragonal phase after the encapsula-

tion process. In the Raman spectral profiles of t-BTO@C shown in Fig. S7,<sup>†</sup> the D peak at  $1343.2\text{ cm}^{-1}$  is associated with structural irregularities or defects within  $\text{sp}^2$ -bonded carbon atoms, and the G peak at  $1570.3\text{ cm}^{-1}$  is linked to the stretching vibration of bonds within the carbon atom faces. The D peak intensity surpasses that of the G peak in t-BTO@C Raman profiles, and it signifies a preponderance of disorder or defects within the  $\text{sp}^2$ -bonded carbon atomic configuration in t-BTO@C.<sup>32</sup> Moreover, the Brunauer–Emmett–Teller (BET) measurement showed that the surface areas of the three samples were similar (Fig. S9<sup>†</sup>). Most of the pore diameters in the three samples were less than  $10\text{ nm}$ , suitable for the pore-filling mechanism of potassium ion storage.<sup>33</sup> The synthesis of t-BTO@C materials is depicted in Fig. 1j, showcasing the t-BTO nanoparticles coated with hard carbon derived from the pyrolysis of polypyrrole.

The potassium storage performance of the t-BTO@C electrode in half-cells was investigated, and the non-ferroelectric  $\text{SiO}_2$ @C and Pure C electrodes serve as references. The t-BTO@C electrode also shows the highest capacity retention after 100 cycles, retaining  $374.9\text{ mA h g}^{-1}$ . In contrast, without ferroelectricity, the  $\text{SiO}_2$ @C electrode and Pure C electrode retain only  $97.2\text{ mA h g}^{-1}$  and  $240.1\text{ mA h g}^{-1}$  capacity (Fig. 2a). Due to the large surface area, all three hard carbon samples show low initial coulombic efficiencies (Fig. 2b).<sup>34</sup> Nevertheless, the coulombic efficiencies can be improved by adjusting the optimization of the carbonization temperature. The coulombic efficiencies of all three samples approach 100% after 20 cycles of activation, suggesting that the hard carbon in the three samples is similar. In Fig. 2c and S10,<sup>†</sup> the galvanostatic charge/discharge profiles at a current density of  $0.05\text{ A g}^{-1}$  reveal the potassiation process in the t-BTO@C electrode. The curve consists of a two-stage potassiation process with a higher slope region ( $>1\text{ V}$ ) from potassium ion adsorption and a lower slope region ( $<1\text{ V}$ ) from potassium ion insertion and pore filling. The decay of capacity in prolonged cycles can be understood from SEI formation (initial few cycles) and ion channel blocking (later cycles).<sup>35</sup> The two-stage potassium storage model was also confirmed from the  $dQ/dV$  curve in Fig. 2d. In the first discharge profile, the  $dQ/dV$  curve exhibits a broad drop between  $0.1$  and  $1\text{ V}$ , which corresponds to the pre-potassiation and SEI formation. Subsequently, the 2nd and 3rd discharge profiles show lesser changes, indicating reversible potassium storage capacity. In the region from  $3$  to  $1\text{ V}$ , the nearly horizontal  $dQ/dV$  curve indicates that the adsorption process only contributes minimal capacity. Meanwhile, the curve shows an increased slope below  $1\text{ V}$ , confirming that most of the capacity is from the insertion-pore filling stage. As the curve is near vertical below  $0.2\text{ V}$ , the majority of the potassiation capacity is probably from the storage of potassium ions in the nanopores of hard carbon.<sup>7</sup>

The rate performance of the t-BTO@C electrode is examined in Fig. 2e. When the current density is increased gradually from  $0.05$  to  $0.1$ ,  $0.2$ ,  $0.5$ ,  $1$ , and  $2\text{ A g}^{-1}$ , the t-BTO@C electrode releases  $461.4$ ,  $390.0$ ,  $359.4$ ,  $326.5$ , and  $288.1\text{ mA h g}^{-1}$  average specific capacity, respectively. Later, when the current



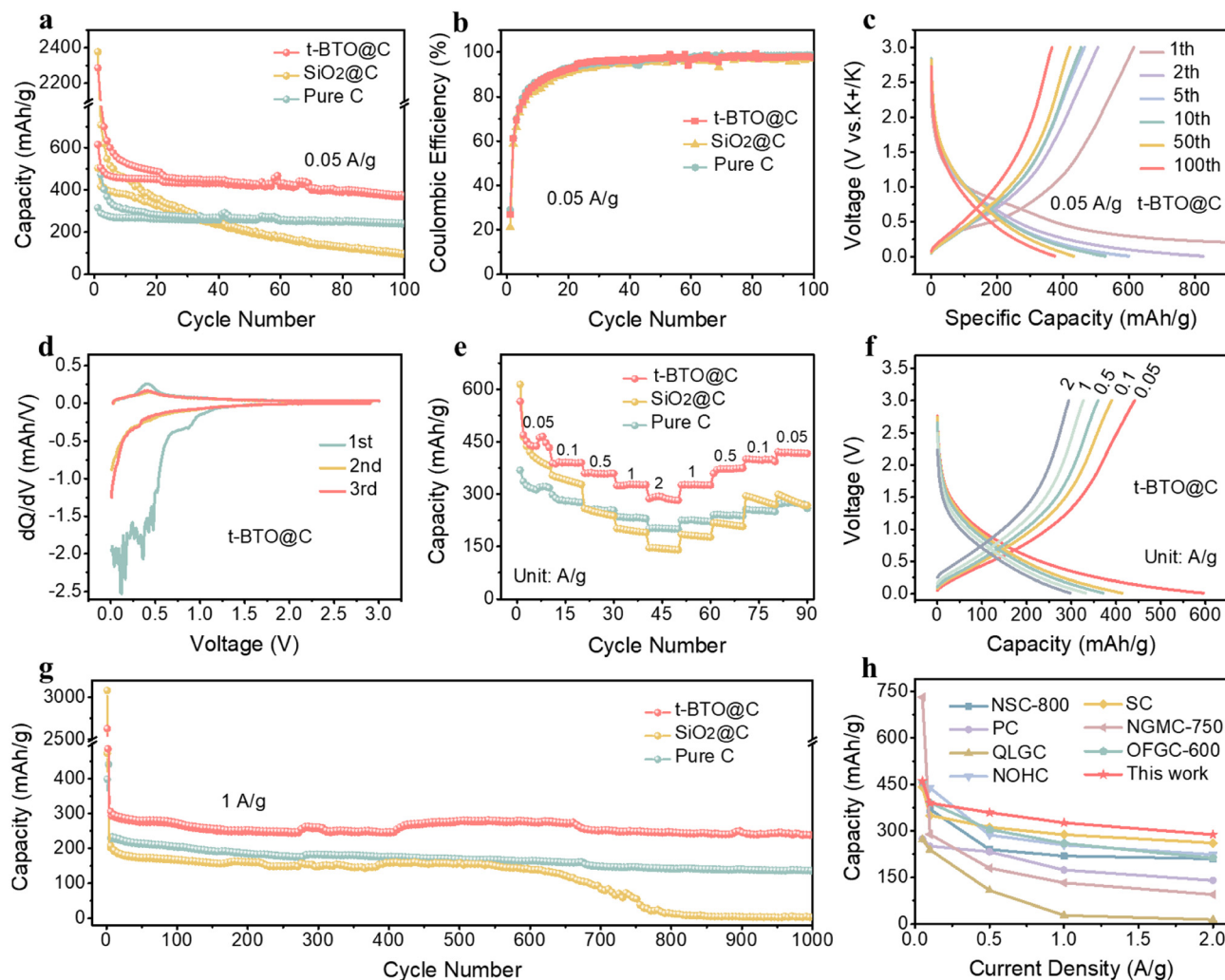


**Fig. 2** (a) Half-cell cycle performances of t-BTO@C, SiO<sub>2</sub>@C, and Pure C electrodes at a current density of 0.05 A g<sup>-1</sup>. (b) Coulomb efficiency of t-BTO@C, SiO<sub>2</sub>@C, and Pure C electrodes at a current density of 0.05 A g<sup>-1</sup>. (c) The galvanostatic charge/discharge profiles of t-BTO@C at a current density of 0.05 A g<sup>-1</sup>. (d) The dQ/dV profile of the t-BTO@C electrode at a current density of 0.01 A g<sup>-1</sup>. (e) Half-cell rate performances of t-BTO@C, SiO<sub>2</sub>@C, and Pure C electrodes at current densities of 0.05, 0.1, 0.5, 1, and 2 A g<sup>-1</sup>. (f) Charge/discharge profiles of rate performances of the t-BTO@C electrode. (g) Half-cell long cycle performances of t-BTO@C, SiO<sub>2</sub>@C, and Pure C electrodes at a current density of 1 A g<sup>-1</sup>. (h) Comparative performance profiles of the t-BTO@C electrode and other electrodes reported in the literature.<sup>10,37–42</sup>

density is reduced from 1 to 0.5, 0.2, 0.1, and 0.05 A g<sup>-1</sup>, the capacities are restored to 326.5, 371.4, 398.9, and 418.6 mA h g<sup>-1</sup>, respectively. In the first cycle, the SiO<sub>2</sub>@C electrode provides an average specific capacity of 430.1 mA h g<sup>-1</sup> at 0.05 A g<sup>-1</sup>. Although the initial specific capacities of SiO<sub>2</sub>@C and t-BTO@C are similar, the SiO<sub>2</sub>@C electrode only has a capacity of 140.9 mA h g<sup>-1</sup> (32.8% of initial capacity) at 2 A g<sup>-1</sup>, while the t-BTO@C electrode shows a higher capacity (288.1 mA h g<sup>-1</sup>, 62.4% of initial capacity) under the same conditions. For the Pure C electrode, the initial capacity is smaller than for the other two samples. The rate performance of the Pure C electrode shows average specific capacities of 325.9, 282.5, 255.6, 233.0, 201.6, 224.1, 239.9, 253.3, and 272.6 mA h g<sup>-1</sup> from 0.05 to 2, and 2 to 0.05 A g<sup>-1</sup>, respectively. The capacity at 2 A g<sup>-1</sup> is 61.9% of the initial capacity, which is still poorer than that of

the t-BTO@C anode. Better kinetics can also be seen by the capacity decay after rate cycles. The remaining capacities of t-BTO@C, SiO<sub>2</sub>@C, and Pure C are 90.8%, 66.5%, and 83.6%, respectively. Therefore, we can conclude that the better potassium ion kinetics improved both the rate performance and the capacity retention after rating cycles. The galvanostatic charge/discharge profiles corresponding to the rate performance of t-BTO@C, SiO<sub>2</sub>@C, and Pure C electrodes are presented in Fig. 2f and S12a–b.† In these profiles, the t-BTO@C electrode shows a larger capacity from the insertion-pore filling stage than those of SiO<sub>2</sub>@C and Pure C. In addition, the long cycling capability of the t-BTO@C electrode at a current density of 1 A g<sup>-1</sup> is shown in Fig. 2g. After 1000 cycles, the t-BTO@C electrode displays a stable reversible specific capacity of 238.2 mA h g<sup>-1</sup>, showing a capacity retention rate of 82.8%



in comparison with the 20th cycle. In contrast, in the  $\text{SiO}_2@\text{C}$  electrode the initial stabilized reversible specific capacity of  $183.2 \text{ mA h g}^{-1}$  drops to near zero after 800 cycles. Although the Pure C electrode can steadily cycle 1000 times, it only shows a specific capacity of  $135.7 \text{ mA h g}^{-1}$  at the end, showing only 60.3% capacity retention, still lower than that of the t-BTO@C electrode. As shown in Fig. 2h, the t-BTO@C electrode also exhibits higher capacity than many other reported hard carbon anodes at large current densities. The better rate performance and cycling stability of the t-BTO@C anode could be explained by the accelerated ion diffusion by the electric field generated from ferroelectric t-BTO particles. The  $P_s$  electrical field could both promote faster diffusion kinetics and increase the amount of potassium ions in the intercalation and pore-filling process.<sup>36</sup>

To reveal the kinetic behavior difference of potassium ions in the three anodes, cyclic voltammetry (CV) measurements were performed as shown in Fig. 3. The CV profiles of t-BTO@C electrodes at different sweep rates are shown in Fig. 3a. The sweep rate is increased from 0.1 to  $1 \text{ mV s}^{-1}$ , and the CV peak currents increase accordingly. Then, the redox peak currents at different sweep rates and the corresponding sweep rates are linearly fitted based on eqn (1) (Fig. S14a†). The calculated  $b_1$  value of the reduction peak is 0.948 and the  $b_2$  value of the oxidation peak is 0.858. In principle, the Faraday current is proportional to  $v^{1/2}$ , and the pseudocapacitance current is proportional to  $v$ . Thus, the redox  $b$  values of the t-BTO@C electrode are between 0.5 and 1, indicating that

the t-BTO@C electrode behaves with Faraday and pseudocapacitance attributes.<sup>43,44</sup>

$$i = av^b \quad (1)$$

In eqn (1),  $a$  and  $b$  are constants,  $i$  is the redox peak current (mA), and  $v$  is the sweep rate ( $\text{mV s}^{-1}$ ). To acquire the contributions of the pseudocapacitive and Faraday current, eqn (1) is converted into eqn (2). The first term ( $k_1v$ ) is attributed to the pseudocapacitance current, and the second term ( $k_2v^{0.5}$ ) is attributed to the Faraday current:

$$i(V) = k_1v + k_2v^{0.5} \quad (2)$$

In eqn (2),  $k_1$  and  $k_2$  are constants,  $i$  is the peak current (mA),  $v$  is the sweep rate ( $\text{mV s}^{-1}$ ), and  $V$  is the specified voltage (V). As depicted in Fig. 3b, the pseudocapacitance contributions to charge storage of the t-BTO@C electrode are 62.5%, 73.7%, 76.5%, 80.9%, and 84.3% at sweep rates of 0.1, 0.3, 0.5, 0.7, and  $1.0 \text{ mV s}^{-1}$ , respectively. Similarly, the pseudocapacitance contributions of the non-ferroelectric  $\text{SiO}_2@\text{C}$  electrode are 59.0%, 71.5%, 74.9%, 79.2%, and 82.1% at sweep rates of 0.1, 0.3, 0.5, 0.7, and  $1.0 \text{ mV s}^{-1}$ , respectively (Fig. S14b–d†). It can be seen that the t-BTO@C electrode always exhibits high percentages of pseudocapacitance contribution. The increased pseudocapacitive contribution at higher sweep rates of the t-BTO@C electrode suggests faster potassium storage capability. In addition, the Galvanostatic Intermittent Titration Technique (GITT) in Fig. 3c shows that

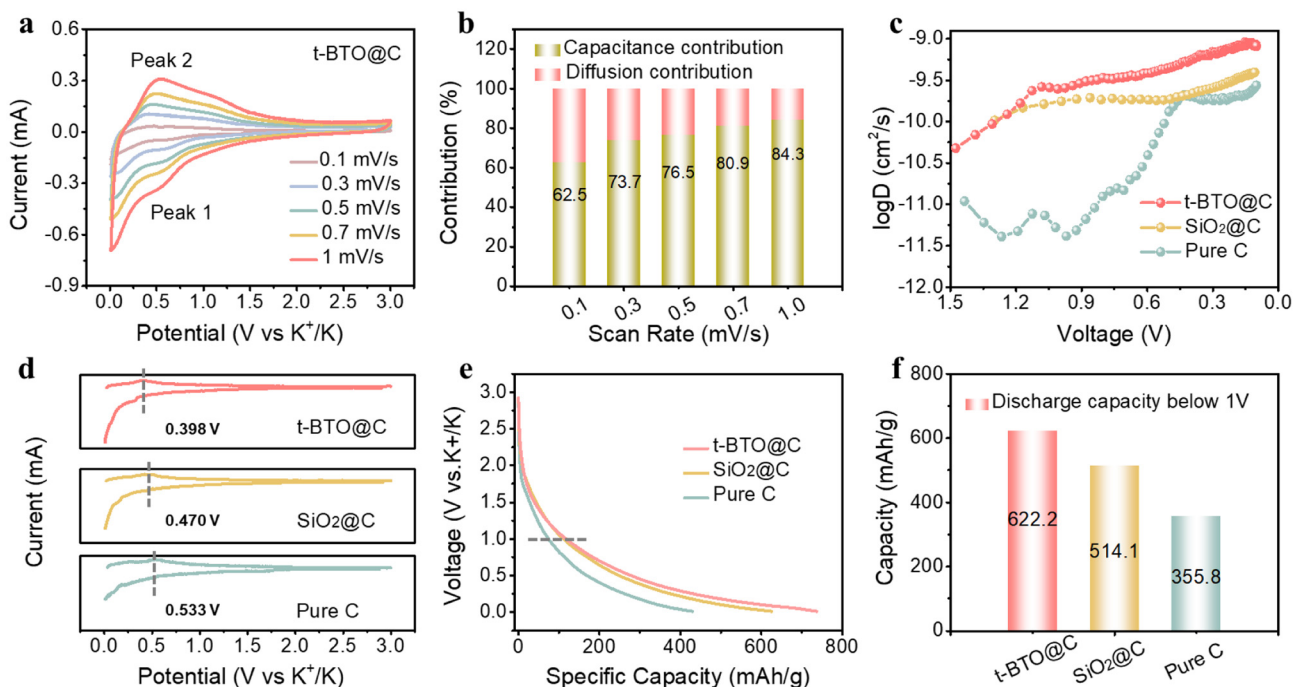


**Fig. 3** (a) Different sweep rates of the CV profile of the t-BTO@C electrode, and (b) different rate capacitive contribution ratios of the t-BTO@C electrode. (c) GITT tests of t-BTO@C,  $\text{SiO}_2@\text{C}$ , and Pure C electrodes. (d) The fourth  $dQ/dV$  profile, (e) the specific capacity–voltage profiles of the fourth cycle, and (f) the corresponding discharge capacity below 1 V of the t-BTO@C,  $\text{SiO}_2@\text{C}$ , and Pure C electrodes at a current density of  $5 \text{ mA g}^{-1}$ .



the t-BTO@C electrode has an average higher ion diffusion coefficient of  $6.95 \times 10^{-10} \text{ cm}^2 \text{ s}^{-1}$ , while those of  $\text{SiO}_2\text{@C}$  and Pure C electrode are  $2.75 \times 10^{-10} \text{ cm}^2 \text{ s}^{-1}$  and  $1.28 \times 10^{-10} \text{ cm}^2 \text{ s}^{-1}$ , respectively. This could be due to the  $P_s$  of t-BTO enhancing the surface adsorption kinetics.<sup>45,46</sup> To illustrate, Fig. 3d presents the  $dQ/dV$  profiles of the fourth cycle. The oxidation potentials of t-BTO@C,  $\text{SiO}_2\text{@C}$ , and Pure C increase from 0.398 V to 0.470 V and 0.533 V, respectively. The large potential suggests larger polarization and slower electron transfer kinetics.<sup>47</sup> During the potassiation process, the t-BTO@C electrode shows a higher current below 0.2 V, while  $\text{SiO}_2\text{@C}$  and Pure C electrodes exhibit a smaller current in this voltage range. The larger current at a lower voltage confirms that the t-BTO@C electrode can accommodate a higher density of potassium ions. To validate this observation, in Fig. 3e the total potassium intercalation capacity of the t-BTO@C,  $\text{SiO}_2\text{@C}$ , and Pure C electrodes have been compared using constant-current discharge curves at  $5 \text{ mA g}^{-1}$ . The t-BTO@C electrode shows a

longer tail in the curve, achieving a discharge capacity of  $622.2 \text{ mA h g}^{-1}$  below 1 V (Fig. 3f), which exceeds the capacities observed in the other  $\text{SiO}_2\text{@C}$  ( $514.1 \text{ mA h g}^{-1}$ ) and Pure C electrodes ( $355.8 \text{ mA h g}^{-1}$ ). From electrochemical measurements, we confirm that the ferroelectric t-BTO@C anode has faster potassiation kinetics with a higher pseudo capacitance contribution and insertion-pore filling stage capacity. Such improvements can be attributed to the enhanced potassium ion migration by the  $P_s$  electric field at the vicinity of t-BTO particles.<sup>48,49</sup>

Efficient and homogeneous migration of potassium ions and rapid charge transfer across interfaces are pivotal factors contributing to the stability and lifetime of PIBs. They can also greatly reduce various side products including the continuously generated SEI layer and other electrolyte byproducts.<sup>50,51</sup> To confirm the positive effect of local ferroelectric particles, the morphology of the t-BTO@C surface was measured by SEM and AFM. Both measurements confirm that the surface has

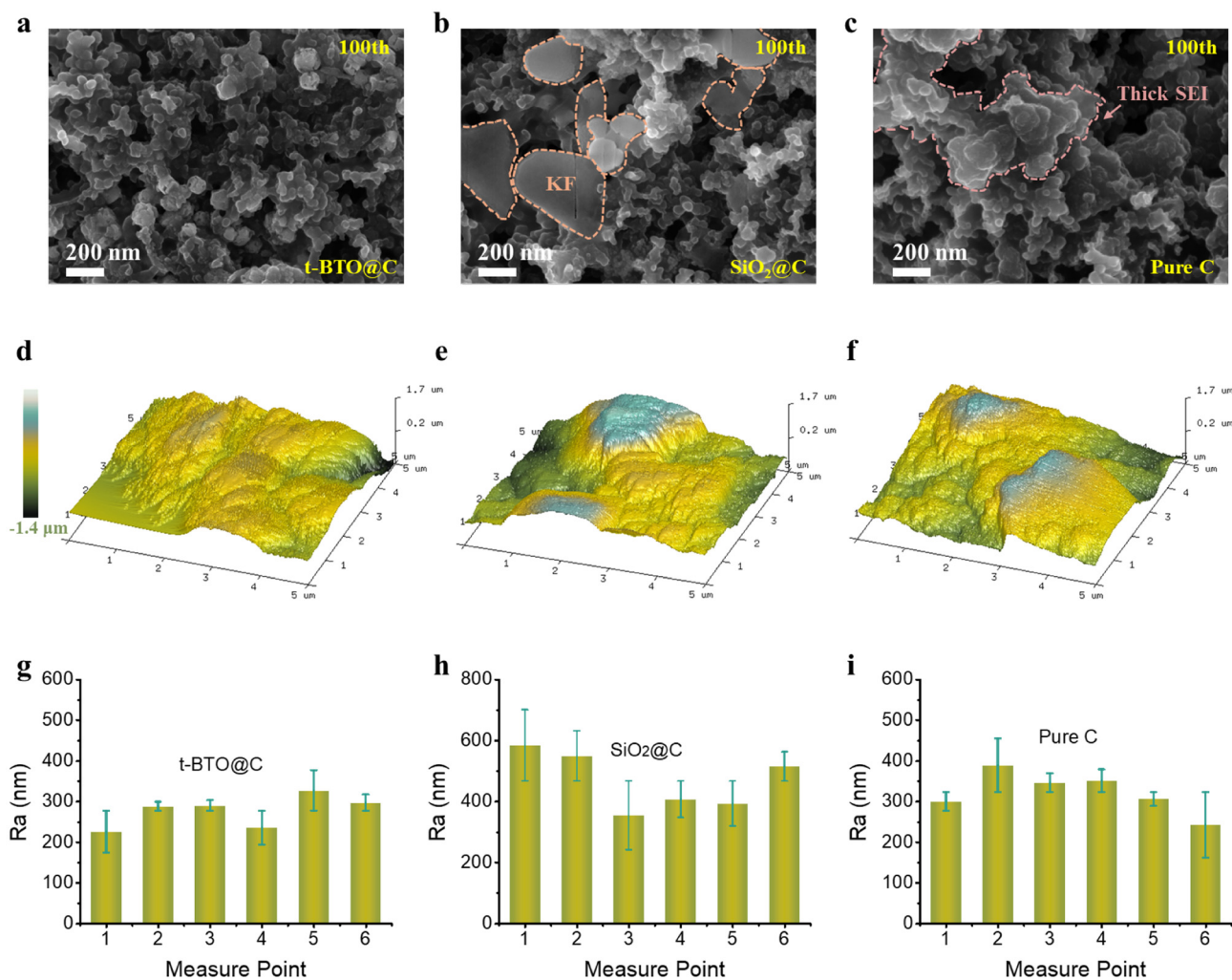


**Fig. 4** SEM image of (a) t-BTO@C, (b)  $\text{SiO}_2\text{@C}$ , and (c) the Pure C electrode surface after 100 cycles at  $0.2 \text{ A g}^{-1}$ . AFM three-dimensional electrode surface altitude morphology map of (d) t-BTO@C, (e)  $\text{SiO}_2\text{@C}$ , and (f) Pure C electrodes after 100 cycles at  $0.2 \text{ A g}^{-1}$ . The  $R_a$  value at different measurement points of (g) t-BTO@C, (h)  $\text{SiO}_2\text{@C}$ , and (i) Pure C electrodes.



fewer byproducts. SEM images depicting the electrode surfaces before the first cycle, and after 50 and 100 cycles, are presented in Fig. 4a–c and Fig. S15a–f.† After 50 cycles, there is a slight increase in the size of t-BTO@C particles, likely attributable to the formation of an SEI layer. In contrast, the average sizes of SiO<sub>2</sub>@C and Pure C particles increase more rapidly, indicating the formation of large amounts of side products. This trend becomes more pronounced after 100 cycles, where bulk potassium fluoride byproducts are observed on SiO<sub>2</sub>@C and Pure C electrodes, suggesting substantial side reactions (Fig. S16–21†). In contrast, the t-BTO@C electrode surface is nearly identical to the pristine surface, indicating minimal side reactions.<sup>52</sup> To examine the actual height changes on these surfaces, atomic force microscopy (AFM) was employed to measure the surface roughness evolution before and after cycling (Fig. 4d–i). After 100 cycles, the t-BTO@C surface exhibits noticeably fewer corrugations compared to the other two electrodes, with the smallest surface roughness ( $R_a$ ) recorded at  $277 \pm 16$  nm. In contrast, the  $R_a$  values are higher at  $467 \pm 38$  nm for SiO<sub>2</sub>@C and  $323 \pm 21$  nm for Pure C electrodes, confirming less roughening of the t-BTO@C surface (Table S1†). The morphological data from SEM and AFM clearly illustrate that the t-BTO@C electrode exhibits minimal byproduct formation in comparison with the electrode with non-ferroelectric SiO<sub>2</sub>@C and Pure C.

We summarize the function of ferroelectric t-BTO particles in the potassiation and depotassiation process in Fig. 5. t-BTO with spontaneous electrical polarization could increase the effective electrical field in the vicinity of hard carbon shells. The average size of t-BTO particles is around 100 nm,

suggesting that these particles can be easily polarized at a voltage as low as 0.35 V (Fig. S22†). During potassiation, the potassium ions are driven by the external electric field and migrate into the hard carbon layer. The t-BTO cores are polarized by the electric field which increases the effective electric field in the hard carbon shells. As a result, the potassiation process is accelerated with less chance of generating byproducts and avoiding the continuous growth of SEI. In the depotassiation process, the  $P_s$  electric field from the t-BTO particle can drive the potassium ion out of the hard carbon layer faster. Such an effect is not available in SiO<sub>2</sub>@C or Pure C anodes. As a result, the potassiation and depotassiation process in t-BTO@C can be performed faster with fewer byproducts and thinner SEI.<sup>36,53–57</sup>

To verify the promising application of the t-BTO@C electrode, a coin full cell with a high-voltage window is prepared using Prussian white as the cathode and t-BTO@C as the anode (Fig. 6a). The PW/t-BTO@C delivers an initial discharge specific capacity of  $356.2 \text{ mA h g}^{-1}$  (based on the anode weight) at a current density of  $0.1 \text{ A g}^{-1}$  as shown in Fig. 6b. After 40 cycles, PW/t-BTO@C shows a discharge specific capacity of  $313.0 \text{ mA h g}^{-1}$ , with 88.9% capacity retention. Furthermore, the PW/t-BTO@C full-cell exhibits discharge specific capacities of 404.7, 371.4, 342.5, 340.1, 307.1, and  $367.3 \text{ mA h g}^{-1}$  at current densities of 0.05, 0.1, 0.2, 0.5, 1, and  $0.05 \text{ A g}^{-1}$ , respectively (Fig. 6c). In Fig. 6d, we compare the full-cell performance of our anode with hard carbon anodes reported recently in the literature under the same conditions. PW/t-BTO@C shows a specific capacity of  $323.0 \text{ mA h g}^{-1}$ ,

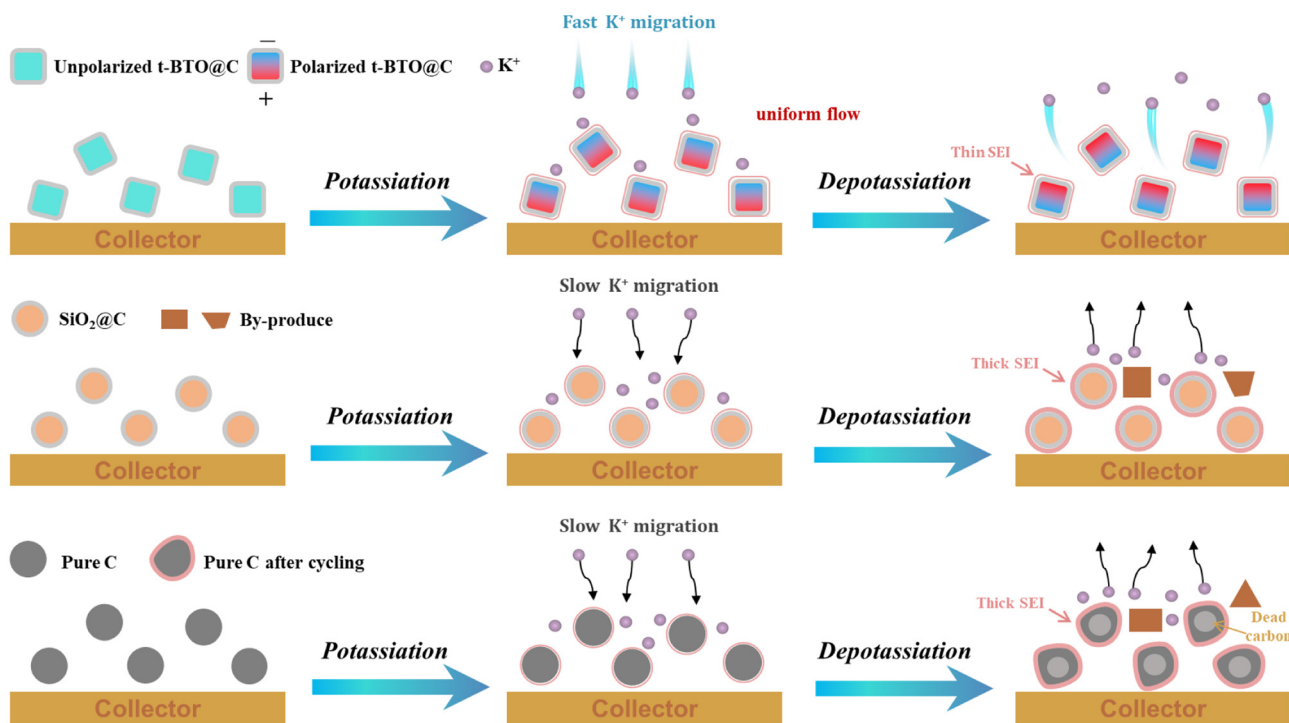
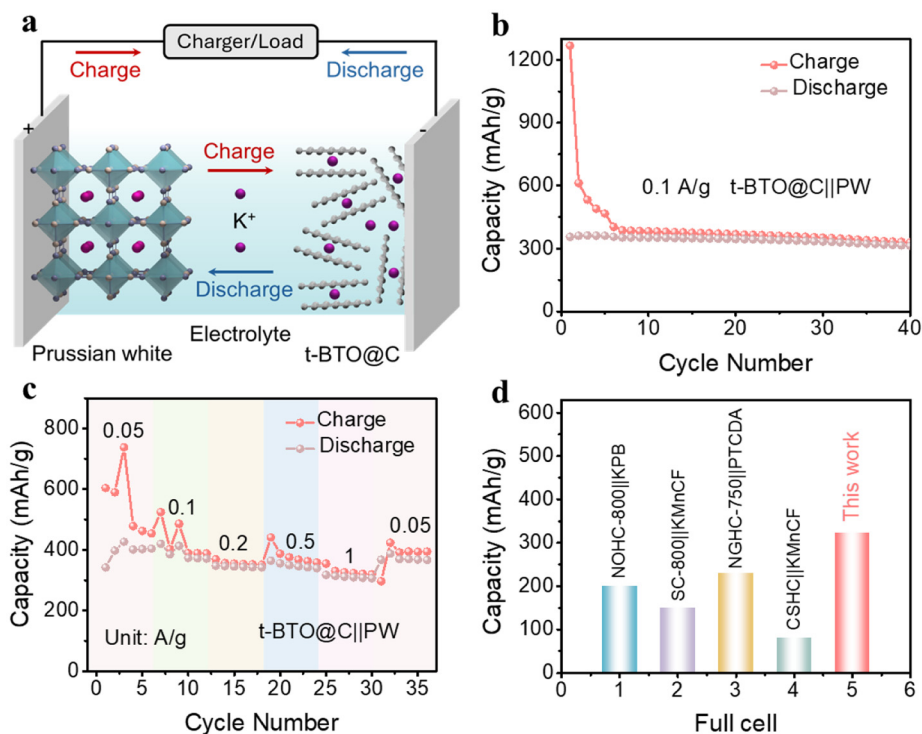


Fig. 5 Schematic diagram of enhanced ion diffusion and capacity by spontaneous polarization electric field in the t-BTO@C electrode, as well as an explanation of the capacity decay and cycling instability of SiO<sub>2</sub>@C and Pure C electrodes.





**Fig. 6** (a) Schematic model of the PW/t-BTO@C full-cell. (b) Cycle performance of the t-BTO@C full-cell at  $0.1 \text{ A g}^{-1}$ . (c) Rate performance of the PW/t-BTO@C full-cell. (d) Comparative cycle performance of the PW/t-BTO@C full-cell and other full-cells reported in the literature at  $0.1 \text{ A g}^{-1}$ .<sup>40–42,58</sup>

much higher than those of other full cells, confirming its outstanding full-cell performance.

## 4. Conclusion

In summary, we fabricated a composite hard carbon anode using t-BTO particles as its core. The t-BTO particles show clear ferroelectric properties with a maximum polarization of  $3.46 \mu\text{C cm}^{-2}$  under a coercive field of  $13.16 \text{ kV cm}^{-1}$ . We confirmed that potassium ions can be driven by the  $P_s$  field of the t-BTO@C anode, enhancing the adsorption of potassium ions in graphitic interlayers. Such effective interaction increased the potassium ion kinetics and the insertion-pore filling potassium storage. The t-BTO@C anode presents  $622.2 \text{ mA h g}^{-1}$  insertion-pore filling capacity, which is higher than the values for  $\text{SiO}_2\text{@C}$  ( $514.1 \text{ mA h g}^{-1}$ ) and Pure C ( $355.8 \text{ mA h g}^{-1}$ ). The  $P_s$  field also homogenizes potassium ion migration, resulting in a uniform SEI layer with less byproduct generation. Therefore, the specific capacity of the t-BTO@C anode achieves  $374.9 \text{ mA h g}^{-1}$  over 100 cycles at  $0.05 \text{ A g}^{-1}$ , which is much higher than the values for  $\text{SiO}_2\text{@C}$  anode ( $97.2 \text{ mA h g}^{-1}$ ) and Pure C anode ( $240.1 \text{ mA h g}^{-1}$ ). The t-BTO@C anode could retain  $238.1 \text{ mA h g}^{-1}$  (82.8% of its capacity) after 1000 cycles at  $1 \text{ A g}^{-1}$ . In addition, the PW/t-BTO@C full-cell exhibits a discharge specific capacity of  $313.0 \text{ mA h g}^{-1}$  at a current density of  $0.05 \text{ A g}^{-1}$  after 40 cycles. Our results reveal an effective strategy to enhance the migration of potassium ions by ferroelectricity.

## Author contributions

Li Rui: conceptualization, methodology, formal analysis, investigation, and writing – original draft. An Keyu: investigation. Ouyang Hao: investigation. Li Heng: methodology, writing – review & editing, supervision, validation. Zhang Yanyan: validation. Tang Yuxin: resources. Liu Jilei: methodology and resources. Chen Shi: writing – review & editing, supervision, project administration, funding acquisition.

## Data availability

The authors declare that the data supporting the findings of this study are available within the paper and its ESI.†

## Conflicts of interest

The authors declare that they have no known competing financial interests or personal relationships that could have appeared to influence the work reported in this paper.

## Acknowledgements

This work was supported by the Macau Science and Technology Development Fund for funding (File No. 0013/



2021/AMJ and 0082/2022/A2), and also partially supported by multi-year research grants (MYRG2022-00266-IAPME and MYRG-GRG2023-00224-IAPME) from the Research & Development Office at the University of Macau. H. Li would like to acknowledge the funding support from the National Natural Science Foundation of China (Grant No. 52202328), the Shanghai Sailing Program (22YF1455500), and the Shanghai Magnolia Talent Program Pujiang Project (24PJD128).

## References

- 1 D. Saurel, B. Orayech, B. Xiao, D. Carriazo, X. Li and T. Rojo, From charge storage mechanism to performance: A roadmap toward high specific energy sodium-ion batteries through carbon anode optimization, *Adv. Energy Mater.*, 2018, **8**, 1703268, DOI: [10.1002/aenm.201703268](https://doi.org/10.1002/aenm.201703268).
- 2 X. Wu, Y. Chen, Z. Xing, C. W. K. Lam, S. Pang, W. Zhang and Z. Ju, Advanced carbon-based anodes for potassium-ion batteries, *Adv. Energy Mater.*, 2019, **9**, 1900343, DOI: [10.1002/aenm.201900343](https://doi.org/10.1002/aenm.201900343).
- 3 X. Wu, D. P. Leonard and X. Ji, Emerging non-aqueous potassium-ion batteries: Challenges and opportunities, *Chem. Mater.*, 2017, **29**, 5031–5042, DOI: [10.1021/acs.chemmater.7b01764](https://doi.org/10.1021/acs.chemmater.7b01764).
- 4 X. Zou, P. Xiong, J. Zhao, J. Hu, Z. Liu and Y. Xu, Recent research progress in non-aqueous potassium-ion batteries, *Phys. Chem. Chem. Phys.*, 2017, **19**, 26495–26506, DOI: [10.1039/c7cp03852f](https://doi.org/10.1039/c7cp03852f).
- 5 X. Wang and H. Wang, Designing carbon anodes for advanced potassium-ion batteries: Materials, modifications, and mechanisms, *Adv. Powder Mater.*, 2022, **1**, 100057, DOI: [10.1016/j.apmate.2022.100057](https://doi.org/10.1016/j.apmate.2022.100057).
- 6 L. Zhang, W. Wang, S. Lu and Y. Xiang, Carbon anode materials: a detailed comparison between Na-ion and K-ion batteries, *Adv. Energy Mater.*, 2021, **11**, 2003640, DOI: [10.1002/aenm.202003640](https://doi.org/10.1002/aenm.202003640).
- 7 Z. Yu, C. Chen, Q. Liu, J. Liu, M. Tang, Y. Zhu and B. Zhang, Discovering the pore-filling of potassium ions in hard carbon anodes: Revisit the low-voltage region, *Energy Storage Mater.*, 2023, **60**, 102805, DOI: [10.1016/j.ensm.2023.102805](https://doi.org/10.1016/j.ensm.2023.102805).
- 8 M. Chen, W. Wang, X. Liang, S. Gong, J. Liu, Q. Wang, S. Guo and H. Yang, Sulfur/oxygen codoped porous hard carbon microspheres for high-performance potassium-ion batteries, *Adv. Energy Mater.*, 2018, **8**, 1800171, DOI: [10.1002/aenm.201800171](https://doi.org/10.1002/aenm.201800171).
- 9 X. Ma, N. Xiao, J. Xiao, X. Song, H. Guo, Y. Wang, S. Zhao, Y. Zhong and J. Qiu, Nitrogen and phosphorus dual-doped porous carbons for high-rate potassium ion batteries, *Carbon*, 2021, **179**, 33–41, DOI: [10.1016/j.carbon.2021.03.067](https://doi.org/10.1016/j.carbon.2021.03.067).
- 10 N. Cheng, W. Zhou, J. Liu, Z. Liu and B. Lu, Reversible oxygen-rich functional groups grafted 3D honeycomb-like carbon anode for super-long potassium ion batteries, *Nano-Micro Lett.*, 2022, **14**, 146, DOI: [10.1007/s40820-022-00892-8](https://doi.org/10.1007/s40820-022-00892-8).
- 11 H. A. Lu, L. A. Wills and B. W. Wessels, Electrical properties and poling of BaTiO<sub>3</sub> thin films, *Appl. Phys. Lett.*, 1994, **64**, 2973–2975, DOI: [10.1063/1.111375](https://doi.org/10.1063/1.111375).
- 12 O. Auciello, J. F. Scott and R. Ramesh, The physics of ferroelectric memories, *Phys. Today*, 1998, **51**, 22–27, DOI: [10.1063/1.882324](https://doi.org/10.1063/1.882324).
- 13 R. Landauer, D. R. Young and M. E. Drougard, Polarization reversal in the barium titanate hysteresis loop, *J. Appl. Phys.*, 1956, **27**, 752–758, DOI: [10.1063/1.1722477](https://doi.org/10.1063/1.1722477).
- 14 J. F. Scott and C. A. P. D. Araujo, Ferroelectric memories, *Science*, 1989, **246**, 1400–1406, DOI: [10.1126/science.246.4936.1400](https://doi.org/10.1126/science.246.4936.1400).
- 15 P. Shi, J. Ma, M. Liu, S. Guo, Y. Huang, S. Wang, L. Zhang, L. Chen, K. Yang, X. Liu, Y. Li, X. An, D. Zhang, X. Cheng, Q. Li, W. Lv, G. Zhong, Y. B. He and F. Kang, A dielectric electrolyte composite with high lithium-ion conductivity for high-voltage solid-state lithium metal batteries, *Nat. Nanotechnol.*, 2023, **18**, 602–610, DOI: [10.1038/s41565-023-01341-2](https://doi.org/10.1038/s41565-023-01341-2).
- 16 H. Y. Sun, H. J. Sohn, O. Yamamoto, Y. Takeda and N. Imanishic, Enhanced lithium-ion transport in PEO-based composite polymer electrolytes with ferroelectric BaTiO<sub>3</sub>, *J. Electrochem. Soc.*, 1999, **146**, 1672–1676, DOI: [10.1149/1.1391824](https://doi.org/10.1149/1.1391824).
- 17 S. Xia, Y. Zhao, J. Yan, J. Yu and B. Ding, Dynamic regulation of lithium dendrite growth with electromechanical coupling effect of soft BaTiO<sub>3</sub> ceramic nanofiber films, *ACS Nano*, 2021, **15**, 3161–3170, DOI: [10.1021/acsnano.0c09745](https://doi.org/10.1021/acsnano.0c09745).
- 18 F. Danzi, M. Valente, S. Terlicka and M. H. Braga, Sodium and potassium ion rich ferroelectric solid electrolytes for traditional and electrode-less structural batteries, *APL Mater.*, 2022, **10**, 031111, DOI: [10.1063/5.0080054](https://doi.org/10.1063/5.0080054).
- 19 J. Wang, Y. Zuo, M. Chen, K. Chen, Z. Chen, Z. Lu and L. Si, Bifunctional separator with a light-weight coating for stable anode-free potassium metal batteries, *Electrochim. Acta*, 2022, **433**, 141211, DOI: [10.1016/j.electacta.2022.141211](https://doi.org/10.1016/j.electacta.2022.141211).
- 20 P. K. Dutta and J. R. Gregg, Hydrothermal synthesis of tetragonal barium titanate, *Chem. Mater.*, 1992, **4**, 843–846, DOI: [10.1021/cm00022a019](https://doi.org/10.1021/cm00022a019).
- 21 H. Meng, Z. Chen, Z. Lu, X. Wang and X. Fu, Hydrothermal synthesis of tetragonal barium titanate nanopowders under moderate conditions, *Process. Appl. Ceram.*, 2021, **15**, 179–183, DOI: [10.2298/pac2102179m](https://doi.org/10.2298/pac2102179m).
- 22 D. Adekoya, H. Chen, H. Y. Hoh, T. Gould, M. J. T. Balogun, C. Lai, H. Zhao and S. Zhang, Hierarchical Co<sub>3</sub>O<sub>4</sub>@N-doped carbon composite as an advanced anode material for ultrastable potassium storage, *ACS Nano*, 2020, **14**, 5027–5035, DOI: [10.1021/acsnano.0c01395](https://doi.org/10.1021/acsnano.0c01395).
- 23 F. Xu, B. Ding, Y. Qiu, R. Dong, W. Zhuang, X. Xu, H. Han, J. Yang, B. Wei, H. Wang and S. Kaskel, Generalized domino-driven synthesis of hollow hybrid carbon spheres with ultrafine metal nitrides/oxides, *Matter*, 2020, **3**, 246–260, DOI: [10.1016/j.matt.2020.05.012](https://doi.org/10.1016/j.matt.2020.05.012).



- 24 Y. Zhang, C. Wang, Y. Zhao, Z. Yu, F. Yang and X. Zhang, Core-shell structured  $\text{Co}_3\text{O}_4@\text{PPy}$  composite for electrochemical determination of terbutylhydroquinone, *RSC Adv.*, 2022, **12**, 29845–29851, DOI: [10.1039/d2ra05574k](https://doi.org/10.1039/d2ra05574k).
- 25 Y. Mo, W. Zhou, K. Wang, K. Xiao, Y. Chen, Z. Wang, P. Tang, P. Xiao, Y. Gong, S. Chen, P. Gao and J. Liu, Engineering electrode/electrolyte interphase chemistry toward high-rate and long-life potassium ion full-cell, *ACS Energy Lett.*, 2023, **8**, 995–1002, DOI: [10.1021/acscenergylett.2c02659](https://doi.org/10.1021/acscenergylett.2c02659).
- 26 R. Ma, Z. Wang, Q. Fu, W. Zhou, Y. Mo, J. Tu, Z. Wang, P. Gao, C. Fan and J. Liu, Dual-salt assisted synergistic synthesis of Prussian white cathode towards high-capacity and long cycle potassium ion battery, *J. Energy Chem.*, 2023, **83**, 16–23, DOI: [10.1016/j.jechem.2023.04.007](https://doi.org/10.1016/j.jechem.2023.04.007).
- 27 U. D. Venkateswaran, V. M. Naik and R. Naik, High-pressure Raman studies of polycrystalline  $\text{BaTiO}_3$ , *Phys. Rev. B: Condens. Matter Mater. Phys.*, 1998, **58**, 21, DOI: [10.1103/PhysRevB.58.14256](https://doi.org/10.1103/PhysRevB.58.14256).
- 28 A. K. Muraleedharan, K. Co, M. Vallet, A. Zaki, F. Karolak, C. Bogicevic, K. Perronet, B. Dkhil, C. Paillard, C. Fiorini-Debuisschert and F. Treussart, Ferroelectric texture of individual barium titanate nanocrystals, *ACS Nano*, 2024, **18**, 18355–18367, DOI: [10.1021/acsnano.4c02291](https://doi.org/10.1021/acsnano.4c02291).
- 29 Y. Wang, L. Tao, R. Guzman, Q. Luo, W. Zhou, Y. Yang, Y. Wei, Y. Liu, P. Jiang, Y. Chen, S. Lv, Y. Ding, W. Wei, T. Gong, Y. Wang, Q. Liu, S. Du and M. Liu, A stable rhombohedral phase in ferroelectric  $\text{Hf}(\text{Zr})_{1+x}\text{O}_2$  capacitor with ultralow coercive field, *Science*, 2023, **381**, 558–563, DOI: [10.1126/science.adf6137](https://doi.org/10.1126/science.adf6137).
- 30 V. S. Babu and M. S. Seehra, Modeling of disorder and X-ray diffraction in coal-based graphitic carbons, *Carbon*, 1996, **34**, 1259–1265, DOI: [10.1016/0008-6223\(96\)00085-1](https://doi.org/10.1016/0008-6223(96)00085-1).
- 31 K. Takai, M. Oga, T. Enoki and A. Taomoto, Effect of heat-treatment on magnetic properties of non-graphitic disordered carbon, *Diamond Relat. Mater.*, 2004, **13**, 1469–1473, DOI: [10.1016/j.diamond.2003.12.020](https://doi.org/10.1016/j.diamond.2003.12.020).
- 32 D. B. Schuepfer, F. Badaczewski, J. M. Guerra-Castro, D. M. Hofmann, C. Heiliger, B. Smarsly and P. J. Klar, Assessing the structural properties of graphitic and non-graphitic carbons by Raman spectroscopy, *Carbon*, 2020, **161**, 359–372, DOI: [10.1016/j.carbon.2019.12.094](https://doi.org/10.1016/j.carbon.2019.12.094).
- 33 A. Rajh, M. Gabrijelčić, B. Tratnik, K. Bučar, I. Arčon, M. Petric, R. Dominko, A. Vizintin and M. Kavčič, Structural and chemical analysis of hard carbon negative electrode for Na-ion battery with X-ray Raman scattering and solid-state NMR spectroscopy, *Carbon*, 2024, **228**, 119398, DOI: [10.1016/j.carbon.2024.119398](https://doi.org/10.1016/j.carbon.2024.119398).
- 34 Y. Guo, Y. Feng, H. Li, Y. Wang, Z. Wen and G. Zhou, Carbon quantum dots in hard carbon: An approach to achieving PIB anodes with high potassium adsorption, *Carbon*, 2022, **189**, 142–151, DOI: [10.1016/j.carbon.2021.12.038](https://doi.org/10.1016/j.carbon.2021.12.038).
- 35 Z. Zhang, G. Huang, X. Qu, Y. Liu, Z. Liu, J. Jia, B. Xing and C. Zhang, An effective strategy to prepare non-graphitic carbon with increased pseudo-graphitic content for sodium-ion battery anode with enhanced plateau capacity, *Chem. Eng. J.*, 2023, **477**, 147188, DOI: [10.1016/j.cej.2023.147188](https://doi.org/10.1016/j.cej.2023.147188).
- 36 R. Li, G. Zhang, P. Zhang, Y. Li, C. He, X. Ren and H. Mi, Accelerating ion transport via *in situ* formation of built-in electric field for fast charging sodium-ion batteries, *Chem. Eng. J.*, 2022, **450**, 138019, DOI: [10.1016/j.cej.2022.138019](https://doi.org/10.1016/j.cej.2022.138019).
- 37 Y. Zhang, W. Wei, C. Zhu, Z. Gao, J. Shi, M. Huang, S. Liu and H. Wang, Interconnected honeycomb-like carbon with rich nitrogen/sulfur doping for stable potassium ion storage, *Electrochim. Acta*, 2022, **424**, 140596, DOI: [10.1016/j.electacta.2022.140596](https://doi.org/10.1016/j.electacta.2022.140596).
- 38 X. Zhang, Z. Lu, L. Qiu, L. Chao, L. Chen, T. Wei, D. Zhang and S. Xu, Molten-salt-induced interpenetrated meso/macro porous structural hard carbon derived from chitosan for enhanced potassium ions storage, *J. Electroanal. Chem.*, 2024, **963**, 118303, DOI: [10.1016/j.jelechem.2024.118303](https://doi.org/10.1016/j.jelechem.2024.118303).
- 39 L. Zhong, W. Zhang, S. Sun, L. Zhao, W. Jian, X. He, Z. Xing, Z. Shi, Y. Chen, H. N. Alshareef and X. Qiu, Engineering of the crystalline lattice of hard carbon anodes toward practical potassium-ion batteries, *Adv. Funct. Mater.*, 2022, **33**, 2211872, DOI: [10.1002/adfm.202211872](https://doi.org/10.1002/adfm.202211872).
- 40 R. C. Cui, B. Xu, H. J. Dong, C. C. Yang and Q. Jiang, N/O Dual-Doped environment-friendly hard carbon as advanced anode for potassium-ion batteries, *Adv. Sci.*, 2020, **7**, 1902547, DOI: [10.1002/advs.201902547](https://doi.org/10.1002/advs.201902547).
- 41 C. Chi, Z. Liu, X. Lu, Y. Meng, C. Huangfu, Y. Yan, Z. Qiu, B. Qi, G. Wang, H. Pang, T. Wei and Z. Fan, Balance of sulfur doping content and conductivity of hard carbon anode for high-performance K-ion storage, *Energy Storage Mater.*, 2023, **54**, 668–679, DOI: [10.1016/j.ensm.2022.11.008](https://doi.org/10.1016/j.ensm.2022.11.008).
- 42 J. Hu, Y. Xie, M. Yin and Z. Zhang, Nitrogen doping and graphitization tuning coupled hard carbon for superior potassium-ion storage, *J. Energy Chem.*, 2020, **49**, 327–334, DOI: [10.1016/j.jechem.2020.03.005](https://doi.org/10.1016/j.jechem.2020.03.005).
- 43 X. Pu, D. Zhao, C. Fu, Z. Chen, S. Cao, C. Wang and Y. Cao, Understanding and calibration of charge storage mechanism in cyclic voltammetry curves, *Angew. Chem., Int. Ed.*, 2021, **60**, 21310–21318, DOI: [10.1002/anie.202104167](https://doi.org/10.1002/anie.202104167).
- 44 T. He, X. Kang, F. Wang, J. Zhang, T. Zhang and F. Ran, Capacitive contribution matters in facilitating high power battery materials toward fast-charging alkali metal ion batteries, *Mater. Sci. Eng., R*, 2023, **154**, 100737, DOI: [10.1016/j.mser.2023.100737](https://doi.org/10.1016/j.mser.2023.100737).
- 45 S. Aderyani, P. Flouda, S. A. Shah, M. J. Green, J. L. Lutkenhaus and H. Ardebili, Simulation of cyclic voltammetry in structural supercapacitors with pseudocapacitance behavior, *Electrochim. Acta*, 2021, **390**, 138822, DOI: [10.1016/j.electacta.2021.138822](https://doi.org/10.1016/j.electacta.2021.138822).
- 46 F. Yuan, Y. Lei, H. Wang, X. Li, J. Hu, Y. Wei, R. Zhao, B. Li, F. Kang and D. Zhai, Pseudo-capacitance reinforced modified graphite for fast-charging potassium-ion batteries, *Carbon*, 2021, **185**, 48–56, DOI: [10.1016/j.carbon.2021.09.008](https://doi.org/10.1016/j.carbon.2021.09.008).
- 47 M. Kim, I. Kim, J. Kim and J. W. Choi, Lifetime prediction of lithium ion batteries by using the heterogeneity of



- graphite anodes, *ACS Energy Lett.*, 2023, **8**, 2946–2953, DOI: [10.1021/acsenergylett.3c00695](https://doi.org/10.1021/acsenergylett.3c00695).
- 48 L. Kitsu Iglesias, E. N. Antonio, T. D. Martinez, L. Zhang, Z. Zhuo, S. J. Weigand, J. Guo and M. F. Toney, Revealing the sodium storage mechanisms in hard carbon pores, *Adv. Energy Mater.*, 2023, **13**, 2302171, DOI: [10.1002/aenm.202302171](https://doi.org/10.1002/aenm.202302171).
- 49 J. Pokharel, A. Cresce, B. Pant, M. Y. Yang, A. Gurung, W. He, A. Baniya, B. S. Lamsal, Z. Yang, S. Gent, X. Xian, Y. Cao, W. A. Goddard, K. Xu and Y. Zhou, Manipulating the diffusion energy barrier at the lithium metal electrolyte interface for dendrite-free long-life batteries, *Nat. Commun.*, 2024, **15**, 3085, DOI: [10.1038/s41467-024-47521-z](https://doi.org/10.1038/s41467-024-47521-z).
- 50 J. Huang, Y. Chen, Z. Cen, T. Yi, M. Liang, Y. Zhu, R. Liu, R. Fu, S. Liu and D. Wu, Topological defect-regulated porous carbon anodes with fast interfacial and bulk kinetics for high-rate and high-energy-density potassium-ion batteries, *Adv. Mater.*, 2024, **36**, 2403033, DOI: [10.1002/adma.202403033](https://doi.org/10.1002/adma.202403033).
- 51 X. Zhou, J. Qi, D. Zhou, T. Li, T. Wu, W. Yang and Y. Xu, In-Built polaronic states self-regulation for boosting potassium-ion diffusion kinetics, *Adv. Funct. Mater.*, 2023, **34**, 2308029, DOI: [10.1002/adfm.202308029](https://doi.org/10.1002/adfm.202308029).
- 52 S. Pan, J. Han, Y. Wang, Z. Li, F. Chen, Y. Guo, Z. Han, K. Xiao, Z. Yu, M. Yu, S. Wu, D. W. Wang and Q. H. Yang, Integrating SEI into layered conductive polymer coatings for ultrastable silicon anodes, *Adv. Mater.*, 2022, **34**, 2203617, DOI: [10.1002/adma.202203617](https://doi.org/10.1002/adma.202203617).
- 53 S. Guo, S. Tan, J. Ma, L. Chen, K. Yang, Q. Zhu, Y. Ma, P. Shi, Y. Wei, X. An, Q. Ren, Y. Huang, Y. Zhu, Y. Cheng, W. Lv, T. Hou, M. Liu, Y.-B. He, Q.-H. Yang and F. Kang, Dissociation mechanism of lithium salt by BaTiO<sub>3</sub> with spontaneous polarization, *Energy Environ. Sci.*, 2024, **17**, 3797–3806, DOI: [10.1039/d4ee00798k](https://doi.org/10.1039/d4ee00798k).
- 54 R. Li, G. Zhang, Y. Wang, Z. Lin, C. He, Y. Li, X. Ren, P. Zhang and H. Mi, Fast ion diffusion kinetics based on ferroelectric and piezoelectric effect of SnO<sub>2</sub>/BaTiO<sub>3</sub> heterostructures for high-rate sodium storage, *Nano Energy*, 2021, **90**, 106591, DOI: [10.1016/j.nanoen.2021.106591](https://doi.org/10.1016/j.nanoen.2021.106591).
- 55 J. Fei, S. Zhao, X. Bo, F. Xie, G. Li, E. A. M. A. Ahmed, Q. Zhang, H. Jin and Z. Lin, Nano-single-crystal-constructed submicron MnCO<sub>3</sub> hollow spindles enabled by solid precursor transition combined Ostwald ripening in situ on graphene toward exceptional interfacial and capacitive lithium storage, *Carbon Energy*, 2023, **5**, e333, DOI: [10.1002/cey2.333](https://doi.org/10.1002/cey2.333).
- 56 S. Zhao, Y. He, Z. Wang, X. Bo, S. Hao, Y. Yuan, H. Jin, S. Wang and Z. Lin, Advancing performance and unfolding mechanism of lithium and sodium storage in SnO<sub>2</sub> via precision synthesis of monodisperse PEG-ligated nanoparticles, *Adv. Energy Mater.*, 2022, **12**, 2201015, DOI: [10.1002/aenm.202201015](https://doi.org/10.1002/aenm.202201015).
- 57 S. Zhao, C. D. Sewell, R. Liu, S. Jia, Z. Wang, Y. He, K. Yuan, H. Jin, S. Wang, X. Liu and Z. Lin, SnO<sub>2</sub> as advanced anode of alkali-ion batteries: Inhibiting Sn coarsening by crafting robust physical barriers, void boundaries, and heterophase interfaces for superior electrochemical reaction reversibility, *Adv. Energy Mater.*, 2019, **10**, 201902657, DOI: [10.1002/aenm.201902657](https://doi.org/10.1002/aenm.201902657).
- 58 L. Tan, J. Chen, L. Wang, N. Li, Y. Yang, Y. Chen, L. Guo, X. Ji and Y. Zhu, High-coulombic-efficiency hard carbon anode material for practical potassium ion batteries, *Batteries Supercaps*, 2024, **7**, 202400010, DOI: [10.1002/batt.202400010](https://doi.org/10.1002/batt.202400010).

